

Article

Investigation of O/N Ordering in Perovskite-Type Oxynitrides $\text{La}_{1-x}\text{Y}_x\text{Ta}(\text{O},\text{N})_3$ on Long Range and Short Scale

Margarida Barroso ¹, Mian Dai ², Cora Bubeck ¹ , Marco Scavini ³ , Gabriel J. Cuello ⁴, Hongbin Zhang ², Anke Weidenkaff ^{1,5}  and Marc Widenmeyer ^{1,*} 

- ¹ Department of Materials- and Geosciences, Materials and Resources, Technische Universität Darmstadt, Peter-Grünberg-Str. 2, 64287 Darmstadt, Germany; anke.weidenkaff@mr.tu-darmstadt.de (A.W.)
- ² Department of Materials- and Geosciences, Theory of Magnetic Materials, Technische Universität Darmstadt, Otto-Berndt-Str. 3, 64287 Darmstadt, Germany; hzhang@tmm.tu-darmstadt.de (H.Z.)
- ³ Department of Chemistry, University of Milan, Via C. Golgi 19, 20133 Milan, Italy; marco.scavini@unimi.it
- ⁴ Institut Laue Langevin, 71 Avenue des Martyrs, 38047 Grenoble, France; cuello@ill.fr
- ⁵ Fraunhofer Research Institution for Materials Recycling and Resource Strategies IWKS, Aschaffener Str. 121, 63457 Hanau, Germany
- * Correspondence: marc.widenmeyer@mr.tu-darmstadt.de

Abstract: Oxynitrides such as $\text{LaTa}(\text{O},\text{N})_3$ are attractive materials as photoelectrodes for photoelectrocatalytic solar water splitting. The potential anionic ordering in their perovskite-type structure has been shown to impact the materials' properties. Given the importance attributed to it, the present study reports a detailed experimental analysis supported by simulations of the anionic ordering of $\text{La}_{1-x}\text{Y}_x\text{Ta}(\text{O},\text{N})_3$. The influence of O/N and yttrium content on the anionic order was assessed. Neutron diffraction analysis was performed on four different nominal compositions— LaTaON_2 , LaTaO_2N , $\text{La}_{0.9}\text{Y}_{0.1}\text{TaON}_2$, and $\text{La}_{0.9}\text{Y}_{0.1}\text{TaO}_2\text{N}$ —at 10 K and 300 K to study potential long-range ordering. Neutron pair distribution function (PDF) analysis was performed on all samples at 10 K and on non-Y-substituted samples at 300 K to evaluate short-range ordering. There was no evidence of long-range O/N order in any of the compounds. In contrast, at a short range ($1.5 \text{ \AA} \leq r < 6 \text{ \AA}$), a $Pnma$ ($a^-b^+a^-$) tilting pattern and local *cis*-ordering of the anions were seen. The latter faded rapidly, leaving the $Pnma$ tilting pattern in a $6 \text{ \AA} \leq r \leq 11 \text{ \AA}$ range. At higher distances, the PDF analysis agreed with the $Imma$ ($a^-b^0a^-$) O/N disordered long-range structure. As the O/N content changed, not much difference in behavior was observed. Yttrium substitution introduced some disorder in the structure; nonetheless, it showed marginal influence on octahedral tilting and anionic ordering.

Keywords: perovskites; oxynitrides; anionic ordering; neutron diffraction; pair distribution function; cluster expansion



Citation: Barroso, M.; Dai, M.; Bubeck, C.; Scavini, M.; Cuello, G.J.; Zhang, H.; Weidenkaff, A.; Widenmeyer, M. Investigation of O/N Ordering in Perovskite-Type Oxynitrides $\text{La}_{1-x}\text{Y}_x\text{Ta}(\text{O},\text{N})_3$ on Long Range and Short Scale. *Inorganics* **2024**, *12*, 90. <https://doi.org/10.3390/inorganics12030090>

Academic Editor: Michael A. Hayward

Received: 17 February 2024

Revised: 10 March 2024

Accepted: 15 March 2024

Published: 18 March 2024



Copyright: © 2024 by the authors. Licensee MDPI, Basel, Switzerland. This article is an open access article distributed under the terms and conditions of the Creative Commons Attribution (CC BY) license (<https://creativecommons.org/licenses/by/4.0/>).

1. Introduction

The conversion of solar energy into a chemical fuel such as hydrogen is attracting attention as a sustainable way to satisfy the world's energy demand. One possible way to achieve it is through photoelectrocatalytic solar water splitting (SWS). The SWS mechanism entails many steps, with the first of them being photon absorption, which requires visible-light-responsive semiconductor materials [1,2].

Mixed anion compounds, especially oxynitrides, are highly interesting because of their diversity of properties such as superconductivity, high dielectric constant, photoluminescence, and photocatalytic activity [3–5]. By (partially) substituting oxygen in precursor oxides, there is a lift of the valence band maximum (VBM) of the materials given that N $2p$ orbitals have higher energy than the O $2p$ ones [1,6]. Thus, oxynitrides typically possess a lower band gap than their corresponding oxides, making them attractive materials as electrodes for SWS [3]. Such an anionic doping process also leads to charge compensation mechanisms, since N^{3-} is introduced in the lattice where only O^{2-} anions are present.

Consequently, a change in the Fermi level and defects in the crystal structure, such as oxygen vacancies, can come as an effect of the partial substitution of oxygen by nitrogen [7]. What results is a link between anionic doping—and hence the anionic ordering—and the electronic structure, which is highly important to understand.

Many oxynitrides, as in the case of $\text{LaTa}(\text{O},\text{N})_3$, have a perovskite-type crystal structure and characteristic formulas such as ABO_2N and ABON_2 , in which A is usually a lanthanide, an alkaline, or an alkaline earth cation, and B is a transition metal cation. In the case of a cubic lattice, cation A is coordinated by 12 anions, and cation B is coordinated by six anions, forming a corner-sharing octahedral $B(\text{O},\text{N})_6$ building block [2,8]. Whether the anions in the ABO_2N and ABON_2 structures are ordered, and if so, what that order is, remain key questions that are being more and more investigated nowadays, as they can largely alter physical properties [3,4].

There are several properties that influence the band gap of oxynitrides, such as the nitrogen content, oxidation state of the cations, and distortion of the octahedral network [3,9–11]. In addition to these factors, strain and anionic ordering are also known to control the band gap [2,12,13]. Thus, the degree of O/N ordering has been gaining attention as a way to tailor oxynitride crystal structures and electric properties [4]. The arrangement of N^{3-} and O^{2-} in the crystal structure highly impacts its material properties, especially the optical and dielectric ones [3], entailing more thorough studies on anionic ordering. According to the literature, anion distributions in oxynitrides have been shown to go from fully ordered [14], to partially ordered [15,16], to completely disordered [17].

LaTaON_2 has been initially reported to show a *trans*-ordering of the anions on a long range [18]. Later studies confirmed the absence of long-range O/N ordering, also based on neutron diffraction data, but a local anionic ordering where layers of disordered *cis*-anion chains are formed in 2D planes, indicating partial O/N ordering as observed, e.g., for BaTaO_2N [19,20], could not be ruled out [3].

This type of ordering has also commonly been observed in the more extensively studied SrTaO_2N , where there is a preferential partial ordering with the $-\text{B}-(\text{O},\text{N})-$ bonds forming *cis*-oriented chains in the equatorial planes of the BO_4N_2 octahedra [5,8,21,22].

One of the motivations of the present paper was to better understand the long-range and short-range anionic ordering of $\text{LaTa}(\text{O},\text{N})_3$, to verify whether there is similar behavior between ABO_2N and ABON_2 , and to gain insight into whether the oxygen and nitrogen content has an influence on the ordering. LaTaO_2N is accessible from nanocrystalline LaTaO_4 , while the ammonolysis of microcrystalline LaTaO_4 results in the formation of LaTaON_2 [23]. However, X-ray diffraction shows a poor contrast between neighboring elements in the periodic table, as is the case of oxygen and nitrogen [24]. Thus, powder neutron diffraction (ND) analysis was performed on LaTaO_2N and LaTaON_2 at temperatures of 10 K and 300 K (room temperature (RT)), and the data were refined using the Rietveld method to identify the best fitting O/N distribution pattern.

Furthermore, in a prior study [10], the potential for band gap tunability was demonstrated in Y-substituted LaTaO_2N , making it the next logical step to analyze the O/N ordering of the material, both on long and short ranges. This would make it possible to understand the impact of ordering on band gap tailoring and the potential correlation between yttrium content and anionic ordering. Thus, powder ND measurements were performed on $\text{La}_{0.9}\text{Y}_{0.1}\text{Ta}(\text{O},\text{N})_3$ at 10 K and RT for the study of anionic ordering in the long range. Additionally, the pair distribution function (PDF) analysis was conducted on LaTaO_2N and LaTaON_2 at 10 K and RT, as well as on $\text{La}_{0.9}\text{Y}_{0.1}\text{Ta}(\text{O},\text{N})_3$ at 10 K, to investigate the short-range O/N ordering.

Moreover, density-functional theory (DFT) calculations were performed to further elucidate the experimental findings. For this, the cluster expansion (CE) method was used, where the energies of representative configurations obtained by DFT are parameterized. Consequential Monte Carlo (MC) simulations were utilized to examine possible phase transitions and associated changes in the anionic ordering with varying temperatures. The focus of the DFT analysis was the experimental crystal structures of the LaTaON_2 perovskite-

type oxynitride, specifically in the space groups *Imma*, *Pnma*, and *Pmn2₁*, selected based on the findings of the PDF analysis.

2. Results and Discussion

2.1. Long-Range Structural Analysis of (La,Y)Ta(O,N)₃

Neutron diffraction analysis was performed on the four samples at both 10 K and 300 K to investigate the presence of anionic ordering in the long range. The measurements at 300 K allowed us to analyze the samples at room temperature in their usual state. The measurements at 10 K were performed to minimize any thermal effects on the lattice, such as thermal vibrations, which can cause atomic displacement. For X-rays, it is well known that such effects can decrease the intensity of the diffracted beams [25]. For neutrons, the coherent scattering length b_c is typically considered to be Q -independent. However, thermal vibrations and atomic displacement/disorder leads to a Debye-Waller-type dampening of the diffraction intensity, as described by B values [26]. Moreover, we aimed to ascertain whether cooling had any influence on the crystal structure before proceeding with pair distribution function analysis at 10 K.

All the neutron diffraction patterns obtained were refined by the Rietveld method [27,28] using the *Fullprof.2k* software (version 6.30) [29] for a better understanding of the long-range O/N order, testing various structural models involving different anionic ordering patterns. Two *trans*-ordered structural models, in space groups *C2/m* and *Imma*, two *cis*-ordered models, *I2₁2₁2* and *Ima2*, and one random-order model, *Imma*, were used. These models were chosen according to Porter et al. [3], who have indicated that LaTaON₂ shows an $a^-b^0a^-$ pattern of octahedral tilting and therefore can adopt any of these anion-ordering models. Additionally, the latter model is in agreement with synchrotron diffraction data presented in a previous study [23]. Firstly, all collected neutron diffraction patterns at 300 K were refined as a random-ordered model in *Imma* using free refinements of the O and N content, while having an overall constraint to an anionic content of 3 and respecting the maximum possible site occupation factor of 1. The results are summarized in Table 1. For LaTaON₂ and La_{0.9}Y_{0.1}TaON₂, within experimental uncertainty, the nominal compositions were confirmed by the refinements. It is important to note that the refinements of the La_{0.9}Y_{0.1}TaO₂N compound revealed that the real composition was La_{0.9}Y_{0.1}TaO_{1.58(7)}N_{1.42(7)}. For LaTaO₂N, the situation remained somewhat unclear as the free refinements strongly pointed to the presence of a N-rich composition. However, in parallel, the B_{iso} values of O(1)/N(1) and O(2)/N(2) were significantly enlarged at the same time, indicating the presence of too much scattering density. This behavior is also in contrast to the observed behavior of LaTaON₂ and La_{0.9}Y_{0.1}TaON₂, where the free refinements of O and N content resulted in significantly lower B values compared to the refinements using fixed compositions. For simplification purposes, the compounds are hereafter solely referred to by their nominal compositions. Secondly, the above-described O/N long-range ordered models were tested and the best-fitting models were determined based on the lowest χ^2 values obtained from the Rietveld refinements, provided that the refinements could be based on physically meaningful parameters.

Table 1. Summary of the nominal compositions and refined O and N content at 300 K using the randomly ordered *Imma* structural model.

Nominal Composition	Refined Composition
LaTaO ₂ N	N/A *
LaTaON ₂	LaTaO _{1.03(6)} N _{1.97(6)}
La _{0.9} Y _{0.1} TaO ₂ N	La _{0.9} Y _{0.1} TaO _{1.58(7)} N _{1.42(7)}
La _{0.9} Y _{0.1} TaON ₂	La _{0.9} Y _{0.1} TaO _{0.98(5)} N _{2.02(5)}

* The refinements were not fully conclusive as they indicated a N-rich composition, while simultaneously, the B_{iso} values of O(1)/N(1) and O(2)/N(2) pointed to a scattering density that was too high.

As an example, the refined neutron diffraction patterns of the 300 K measurements are illustrated in Figure 1a–d. The refined patterns of the 10 K measurements can be found in the Supplementary Materials (Figure S1a–d). The refined results are summarized in Table S1.

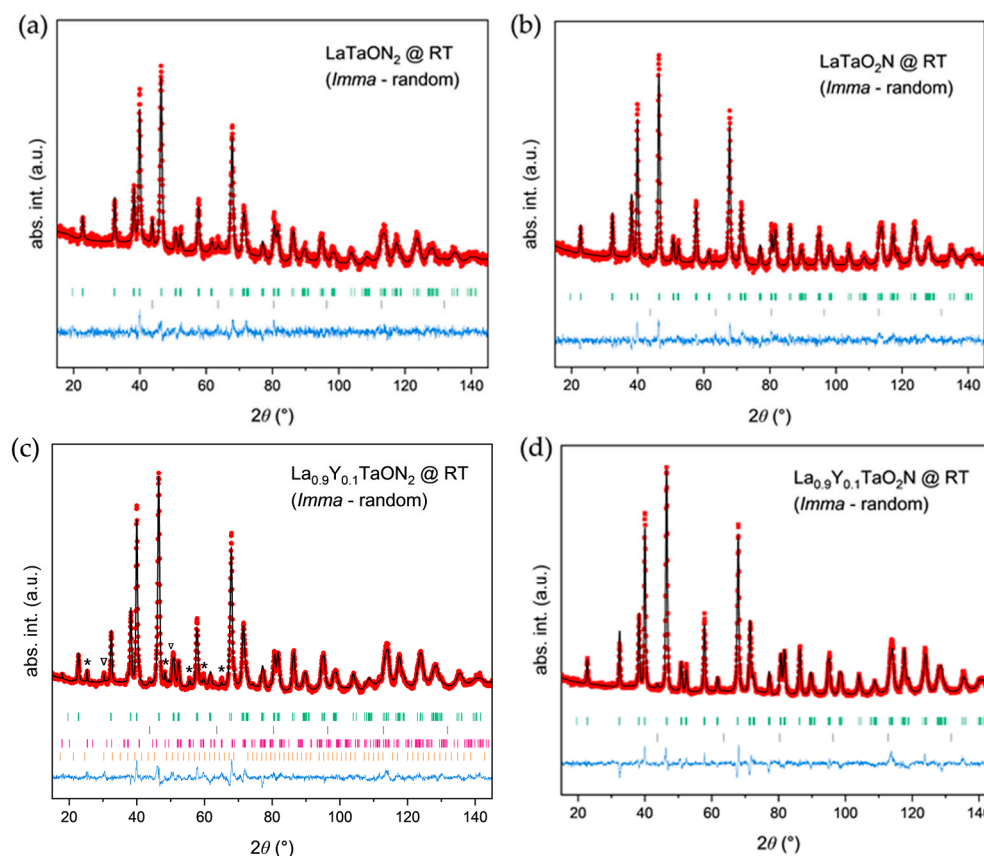


Figure 1. Refined neutron diffraction ($\lambda = 1.59417(2) \text{ \AA}$) patterns of (a) LaTaON_2 , (b) LaTaO_2N , (c) $\text{La}_{0.9}\text{Y}_{0.1}\text{TaON}_2$, and (d) $\text{La}_{0.9}\text{Y}_{0.1}\text{TaO}_2\text{N}$ at 300 K using the *Imma* random anionic ordering structural model. The red dots represent the experimental data, the black line the calculated pattern, and the blue line the difference curve. Green hash marks represent the indexed reflections of the oxynitrides and gray hash marks the indexed reflections of the vanadium sample holder. Pink hash marks in (c) represent the indexed reflections of Ta_3N_5 , and yellow hash marks the indexed reflections of Y_2O_3 . Additionally, the reflections of Ta_3N_5 and Y_2O_3 are marked with * and ∇ , respectively, in (c), for consistency with Figure S1c.

The nominal compositions of the materials and the different tested structural models used for refinements at 10 K and 300 K are summarized in Table 2, along with the corresponding χ^2 values.

By observation of the χ^2 values presented in Table 2, it is evident that the disordered structural refinements using the *Imma* random structural model provided the best fit for all compositions as indicated by the lowest numbers. This is evidence that there is no long-range O/N order in the measured (La,Y)Ta(O,N)₃ materials. It is important to note that although some of the χ^2 values are lower for other structural models on some of the samples, these values were obtained by refinements that involved non-physically meaningful parameters, such as a negative B_{iso} -value, which is the isotropic, temperature-dependent Debye-Waller atomic displacement parameter. Nevertheless, these refinements of alternative structural models have been included for completeness. All refinements were carried out in a manner to maintain consistency in the number of free parameters, ensuring a reasonable comparison between the different refinement models.

Table 2. Summary of the χ^2 values obtained in Rietveld refinements of the neutron diffraction patterns of all samples at 10 K and 300 K using different structural models. The lowest values obtained by refinements based on physically meaningful parameters are highlighted in bold. N/A refers to the fact that since the real composition of the compound was $\text{La}_{0.9}\text{Y}_{0.1}\text{TaO}_{1.58(7)}\text{N}_{1.42(7)}$, the structural model was non-applicable.

Nominal Composition	T (K)	<i>C2/m</i> (<i>trans</i> -Ordered)	<i>I212121</i> (<i>cis</i> -Ordered)	<i>Ima2</i> (<i>cis</i> -Ordered)	<i>Imma</i> (Random)	<i>Imma</i> (<i>trans</i> -Ordered)
LaTaO ₂ N	10	3.39 #	6.19 #	3.87	2.58	3.67
	300	3.09 #	8.42 #	3.31 #	2.14	2.78
LaTaON ₂	10	1.25 #	2.33 #	1.35 #	0.13	1.27 #
	300	0.999 #	1.65 #	0.995 #	1.04	0.945 #
La _{0.9} Y _{0.1} TaO ₂ N	10	N/A	N/A	N/A	2.58	N/A
	300	N/A	N/A	N/A	2.14	N/A
La _{0.9} Y _{0.1} TaON ₂	10	4.04 #	8.73	3.91	3.29	3.64 #
	300	4.65 #	9.61	5.27	3.72	3.99 #

The refinements involved non-physically meaningful parameters.

However, it has been shown that in some materials, although there is no long-range O/N order, there is intermediate anionic ordering characterized by local clustering that can generate well-ordered local anion arrangements [2]. An example of such local ordering, most frequently observed in SrTaO₂N and some LaTaON₂ studies, is the formation of layers of zig-zag Ta–N chains that lead to local *cis*-N–Ta–N configurations. Porter et al. [3] explained that *cis*-configurations are favored over *trans*-configurations because of lower lattice enthalpies in the former. Additionally, the propensity for a *cis*-configuration does not result in long-range anionic ordering because there are numerous distinct *cis*-ordered structures with similar enthalpies.

To shed light on the experimental findings, we performed theoretical investigations combining DFT calculations, CE modelling, and Monte Carlo simulations. Focusing on the experimental crystal structures of LaTaON₂, a set of 300 configurations was generated, featuring randomly distributed O/N atoms within a 40-atom supercell. These configurations were uniquely crafted to ensure energetic distinctiveness, eliminating the possibility of symmetrical equivalence between any two randomly created configurations. Figure 2 depicts the *Imma* crystal structure of LaTaON₂, where orbit indices 2, 3, 4, and 5 represent the possible first-nearest-neighbor (1NNs) configurations of N–N, N–O, and O–O; while orbit indices 8, 9, and 10 represent the possible second-nearest-neighbor (2NNs) configurations of N–N, N–O, and O–O. The experimental lattice parameters were $a_{\text{exp}} = 5.701 \text{ \AA}$, $b_{\text{exp}} = 8.041 \text{ \AA}$, and $c_{\text{exp}} = 5.736 \text{ \AA}$ and the calculated lattice parameters were identical, except for $c_{\text{calc}} = 5.707 \text{ \AA}$.

Our DFT calculations were performed using the augmented plane wave method as implemented in the Vienna Ab initio Simulation Pack (VASP) [30,31], where the total energies of all 300 configurations were evaluated after full geometric optimization. The DFT-calculated energies of the randomly generated configurations were then fed into the CE models through linear fitting, utilizing the automatic relevance detection regression (ARDR) algorithm implemented within the integrated cluster expansion toolkit (ICET) [32]. The results of this fitting of the elective cluster interactions can be seen in Figure S2. The Monte Carlo simulations were conducted using the MCHAMMER module of ICET. A significantly larger $12 \times 12 \times 12$ supercell was employed for these simulations, operating in the canonical ensemble. We adopted a simulated annealing procedure, where the temperature was gradually decreased from 2000 K to 0 K at a rate of 100 K per 100,000 MC cycles. Throughout these simulations, monitoring of cluster counts was maintained to provide statistical insight into the distribution and interaction between O and N occupations.

Moreover, it facilitated the characterization of the temperature-dependent behavior of the nearest neighbors for specific species.

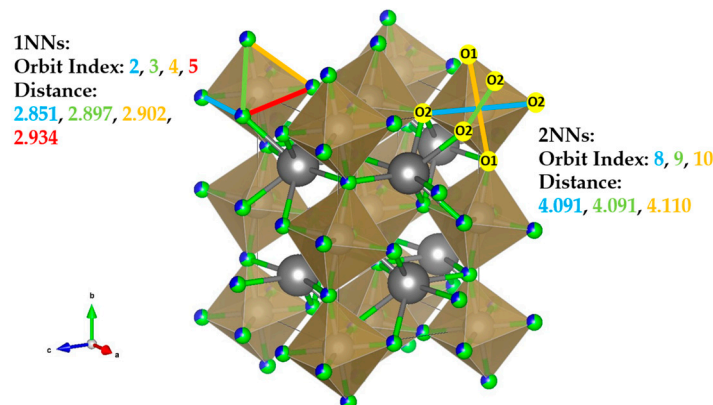


Figure 2. Symmetrically non-equivalent two-body clusters in the cluster expansion of the total energy as a function of O/N occupation in *Imma* LaTaON₂. Orbit indices 2, 3, 4, and 5 represent the N–N, N–O, and O–O possible first-nearest-neighbor (1NNs) configurations, and orbit indices 8, 9, and 10 represent the N–N, N–O, and O–O possible second-nearest-neighbor (2NNs) configurations. The gray ions represent lanthanum, the blue/green ions represent the anions, oxygen and nitrogen, and the ions inside the octahedral structure represent tantalum. O1 and O2 represent, respectively, the N(1)/O(1) and N(2)/O(2) positions of the anions, oxygen and nitrogen.

The Monte Carlo results displayed in Figure 3a indicate that there is no preference for the nitrogen ions to occupy a specific Wyckoff position in the structure of LaTaON₂. This supports the observation based on the neutron diffraction analysis above, which indicates that the disordered *Imma* structure is preferred in LaTaON₂. Furthermore, as seen in Figure 3b, the number of two-body N–N clusters in the second-nearest-neighbor configuration—represented by indices 8, 9, and 10—approaches much lower numbers when compared to the number of two-body N–N clusters in the first-nearest-neighbor configuration—represented by indices 2, 3, and 4—including at our material’s synthesis temperature of $T = 1275$ K. This indicates that the propensity for a *cis*-configuration in LaTaON₂ was confirmed by the MC simulations.

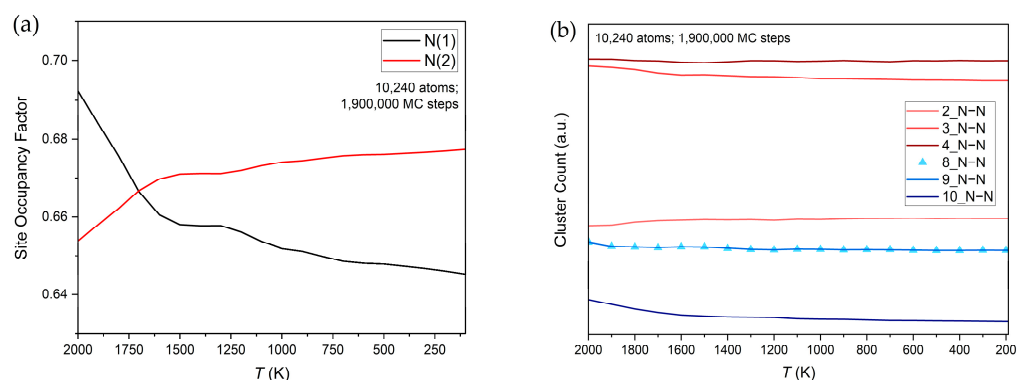


Figure 3. (a) The N site occupancy factors at two non-equivalent sites at different temperatures; (b) numbers of specific two-body clusters of *Imma* LaTaON₂ at different temperatures.

Thus, a pair distribution function (PDF) analysis was performed for a better understanding of the anionic order in (La,Y)Ta(O,N)₃. Various structural models were tested for all samples at 10 K and for the LaTa(O,N)₃ ones at 300 K. Different tilting and O/N ordering patterns at diverse length scales were tested. The best-fitting models were chosen based on the lowest R_w values obtained from the pattern refinements.

2.2. Short-Range Structural Analysis of $(La,Y)Ta(O,N)_3$

2.2.1. $LaTaON_2$ and $LaTaO_2N$

First, a definition of three models is vital for the analysis of the PDF data. A “disordered” model as observed from the neutron diffraction refinements on a long range is one where O and N share both sites with a 0.333/0.667 ratio in the case of $LaTaON_2$ and a $\sim 0.667/0.333$ ratio in the case of $LaTaO_2N$; an “ordered” model corresponds to one where the N(1) site is occupied only by oxygen; and an “inverse-ordered” model describes a situation where the N(1) site is occupied only by nitrogen atoms.

The best fit in $LaTaON_2$ at 10 K for the average structure (space group: $Imma$) with a disordered model can be seen in Figure 4a.

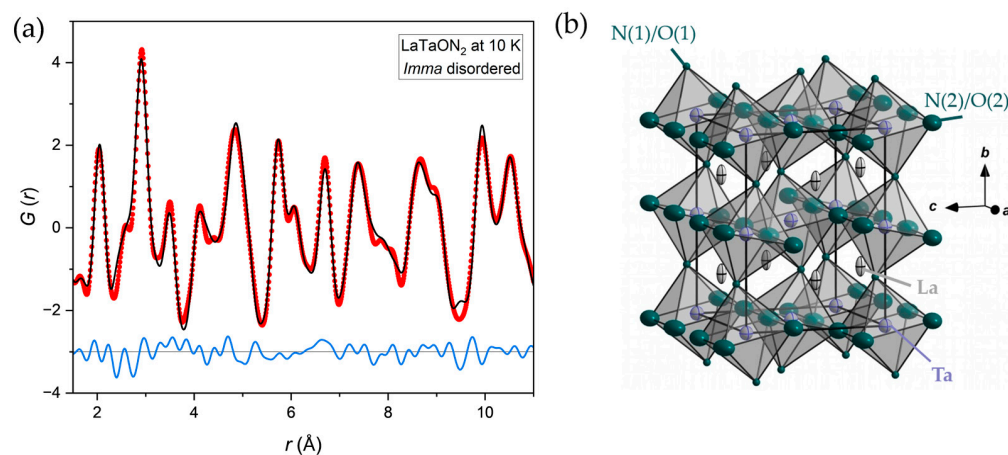


Figure 4. (a) Best fitting PDF pattern for the average structure of $LaTaON_2$ at 10 K, with the space group $Imma$, a disordered model, and using the $U(La,O(2)/N(2))_{aniso}$ thermal parameters, where the red dots represent experimental data, the black line the calculated pattern, the blue line the difference curve, and the gray line is the offset zero line of the difference curve as serves as a guide to the eye; (b) section of the crystal structure of $LaTaON_2$ at 10 K using the same model, where the light gray ellipsoid ions represent lanthanum, the purple ions represent the tantalum, the small spherical green ions represent the N(1)/O(1) positions of the anions, oxygen and nitrogen, and the large ellipsoid green ions represent the N(2)/O(2) positions of the anions.

Then, different models were tested, setting selected (or all) U values as anisotropic. The fit quality improved only when the $U(La)$ and $U(O(2)/N(2))$ thermal parameters were considered anisotropic, different to the $U(Ta)$ and $U(O(1)/N(1))$ case. In addition, no ellipsoid elongation was observed in the last two cases. To avoid having too many parameters and correlations among them, in the following refinements only, the $U(La)$ and $U(O(2)/N(2))$ thermal parameters were set as anisotropic. This fit resulted in the R_w values seen in Table 3, for both $LaTaON_2$ and $LaTaO_2N$. When trying to introduce other models or other kinds of thermal parameters, no significant improvements in R_w values were observed, as shown in Table S2.

By observation of the crystal structure of $LaTaON_2$ with the $U(La,O(2)/N(2))_{aniso}$ thermal parameters and space group $Imma$, seen in Figure 4b, it was possible to distinguish elongated ellipsoids of the $(O(2)/N(2))$ sites along the b -axis. This could indicate either a positional disorder on the $O(2)/N(2)$ site, implying different N–Ta–N, N–Ta–O, and O–Ta–O bond angles in the structure, or tilting along the b -axis.

All the anionic ordering patterns, both *trans*-($Imma$ and $C2/m$) and *cis*-($Ima2$ and $I2_12_12_1$), as described in Porter et al. [3], were tested, resulting in higher R_w values and indicating a lack of order in the fitting range of up to 11 Å in any of these models. This, along with the disordered $Imma$ structure R_w values shown in Table 4 for more expanded r ranges, corroborates the previous conclusion drawn from the neutron diffraction analysis, which ruled out the possibility of long-range ordering.

Table 3. R_w values obtained using three distinct models in the PDF analysis for both LaTaON₂ and LaTaO₂N at 10 K, in the short ($1.5 \text{ \AA} \leq r \leq 5.5 \text{ \AA}$) and wider ($1.5 \text{ \AA} \leq r \leq 11 \text{ \AA}$) ranges. The lowest values obtained for each composition are highlighted in bold.

Compound	Model	R_w ($1.5 \text{ \AA} - 5.5 \text{ \AA}$)	R_w ($1.5 \text{ \AA} - 11 \text{ \AA}$)
LaTaON ₂	<i>Imma</i> _disordered	0.117	0.144
	<i>Pnma</i> _inverse-ordered	0.102	0.132
	<i>Pmn</i> 2 ₁ _along- <i>c</i> -axis	0.092	0.129
LaTaO ₂ N	<i>Imma</i> _disordered	0.138	0.181
	<i>Pnma</i> _inverse-ordered	0.121	0.156
	<i>Pmn</i> 2 ₁ _along- <i>c</i> -axis	0.107	0.151

Table 4. R_w values obtained using three distinct models in the PDF analysis for LaTaON₂ at 10 K, in 6 different ranges, going from shorter to longer ranges. The lowest obtained values for each range are highlighted in bold.

Model	R_w ($1.5 \text{ \AA} - 5.5 \text{ \AA}$)	R_w ($1.5 \text{ \AA} - 8.2 \text{ \AA}$)	R_w ($1.5 \text{ \AA} - 11 \text{ \AA}$)	R_w ($5 \text{ \AA} - 15 \text{ \AA}$)	R_w ($10 \text{ \AA} - 20 \text{ \AA}$)	R_w ($15 \text{ \AA} - 25 \text{ \AA}$)
<i>Imma</i> _disordered_ U_{iso}	0.146	0.211	0.195	0.188	0.268	
<i>Imma</i> _disordered_ U_{aniso} (La,N(2))	0.117	0.143	0.144	0.132	0.185	0.179
<i>Pnma</i> _inverse-ordered_ U_{iso}	0.102	0.137	0.132	0.149	0.192	0.214

For both compositions, LaTaON₂ and LaTaO₂N, at 10 K, the addition of in-phase rotation of the octahedra in the perovskite-type structure along the *b*-axis brought a good fit, as depicted in Figure 5a,b.

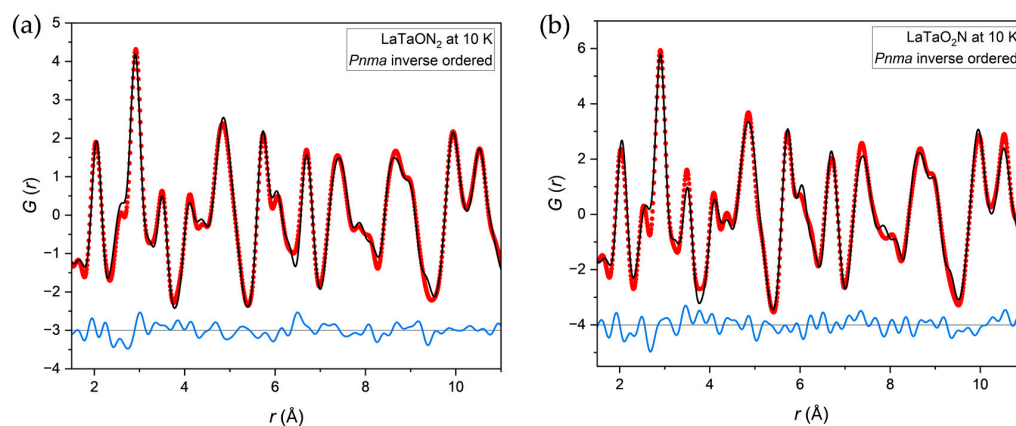


Figure 5. PDF pattern fits of (a) LaTaON₂ at 10 K and (b) LaTaO₂N at 10 K, in the $1.5 \text{ \AA} \leq r \leq 11 \text{ \AA}$ range, obtained after the addition of in-phase rotation of the octahedra along the *b*-axis, leading to the space group *Pnma* and inverse-ordered models. The red dots represent experimental data, the black line the calculated pattern, the blue line the difference curve, and the gray line is the offset zero line of the difference curve as serves as a guide to the eye.

The N/O site occupation was allowed to fluctuate, resulting in inverse-ordered models. After introducing tilting along the *b*-axis, only isotropic thermal parameters were necessary, and the difference between the O(1)/N(1) and O(2)/N(2) thermal parameters was the smallest using this model, with $U(O(1)/N(1))_{iso} = 0.004(1) \text{ \AA}^2$ and $U(O(2)/N(2))_{iso} = 0.010(2) \text{ \AA}^2$ for LaTaON₂, and $U(O(1)/N(1))_{iso} = 0.003(1) \text{ \AA}^2$ and $U(O(2)/N(2))_{iso} = 0.008(2) \text{ \AA}^2$ for

LaTaO₂N. This fit revealed a *Pnma* ($a^-b^+a^-$) tilting pattern, with R_w values that can be seen in Table 3 for both compositions.

However, noticeable differences can be seen in the fit in the $2.2 \text{ \AA} \leq r \leq 3 \text{ \AA}$ interval, which could indicate the confinement of oxygen at the N(2) site; leading to a hidden order at a local scale. Applying, in LaTaON₂, local O/N ordering along the *c*-axis, with the formation of alternate ...-N-N-N-... and ...-O-O-O-... rows running along either the *c*- or the *a*-axis, as shown in Figure 6a, resulted in the best fit in the local range. With this model, each octahedron had an edge formed by two oxygen ions in the *ac* plane, and the lattice symmetry should be changed to *Pmn2*₁. However, to reduce the number of variable parameters, the symmetry constraints and axis orientations of *Pnma* were maintained and only the shift of the tantalum atom towards the N-N edge was introduced here as one degree of freedom.

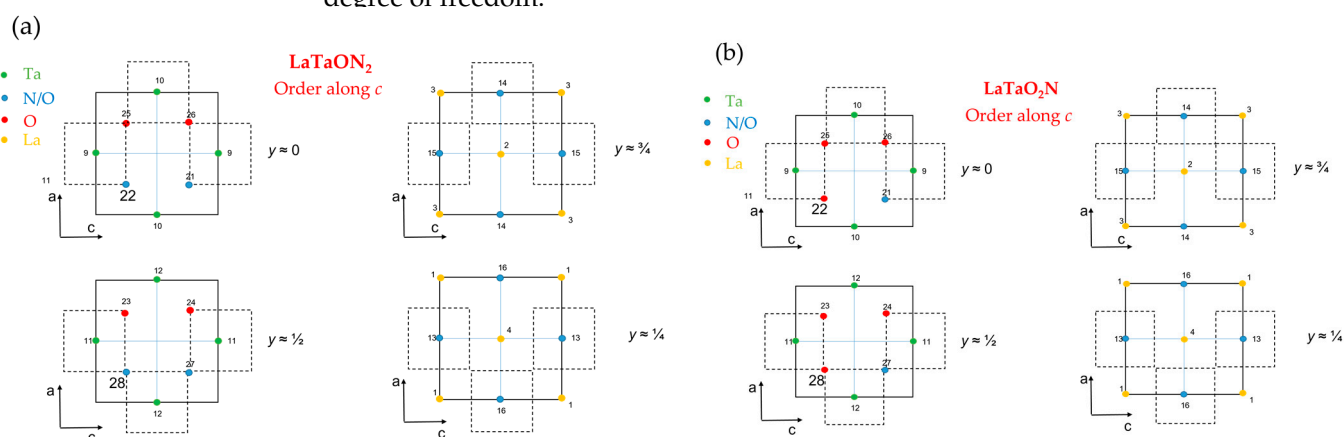


Figure 6. Representations of the atomic structures of (a) LaTaON₂ and (b) LaTaO₂N ordered along the *c*-axis. Space group: *Pmn2*₁. The dashed lines represent the equatorial planes of the octahedra.

For LaTaO₂N, the same structure was applied by simply exchanging the O/N ratio and turning positions 22 and 28 from nitrogen atoms into oxygen atoms, as seen in Figure 6b, and this model also resulted in the best fit.

The fits obtained after applying the aforementioned models can be seen in Figures 7b and 8b. The R_w values obtained are represented in Table 3, and $U(O(1)/N(1)) = U(O(2)/N(2))$ was introduced as a constraint for both compositions to reduce the number of fluctuating parameters, implying equal disorder on both sites.

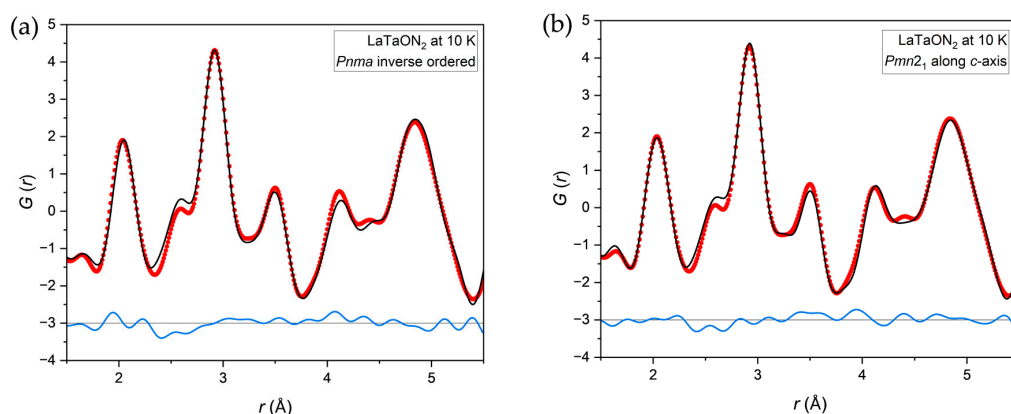


Figure 7. PDF pattern fits of (a) LaTaON₂ at 10 K, with in-phase rotation of the octahedra along the *b*-axis, space group *Pnma*, and an inverse-ordered model, and (b) LaTaO₂N at 10 K, with the addition of local O/N ordering along the *c*-axis and space group *Pmn2*₁. Both were in a $1.5 \text{ \AA} \leq r \leq 5.5 \text{ \AA}$ range. The red dots represent experimental data, the black line the calculated pattern, the blue line the difference curve, and the gray line is the offset zero line of the difference curve as serves as a guide to the eye.

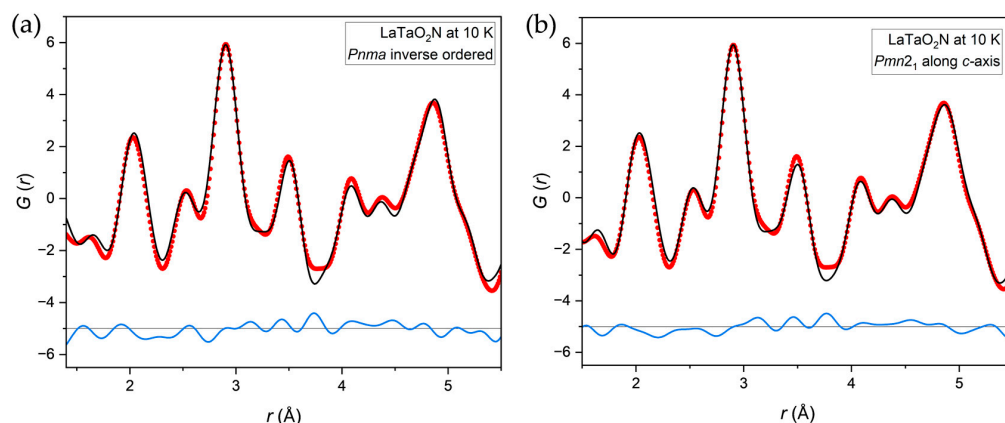


Figure 8. PDF pattern fits of (a) LaTaO₂N at 10 K, with in-phase rotation of the octahedra along the *b*-axis, space group *Pnma*, and an inverse-ordered model, and (b) LaTaO₂N at 10 K, with the addition of local O/N ordering along the *c*-axis and space group *Pmn*2₁. Both were in a 1.5 Å ≤ *r* ≤ 5.5 Å range. The red dots represent experimental data, the black line the calculated pattern, the blue line the difference curve, and the gray line is the offset zero line of the difference curve as serves as a guide to the eye.

Figures 7a and 8a represent a scaling down of the fits using the *Pnma* model seen in Figure 5a,b to the 1.5 Å ≤ *r* ≤ 5.5 Å range for better comparison.

By putting the *Pnma* inverse-ordered models side by side with the models ordered along the *c*-axis, a fit improvement was observed in the 2.2 Å ≤ *r* ≤ 3 Å interval of the latter model (Figures 7b and 8b) for both compounds. Furthermore, although there was a lower improvement in the fit in the widest range of LaTaON₂, the *R_w* of both materials was clearly lower in the shortest range when compared, as seen in Table 3.

As an overview, for both LaTaON₂ and LaTaO₂N, the best fit expressed by the lowest *R_w* values for the wider (*r* < 11 Å) and shorter (*r* < 5.5 Å) ranges was obtained by the *Pmn*2₁ model, which indicated a *Pnma* (*a*[−]*b*⁺*a*[−]) tilting pattern and local *cis*-ordering of the anions along the *c*-axis. However, in both cases, the *R_w* values of the *Pnma* and *Pmn*2₁ models became closer in the widest fitting range, indicating a dampening of the *cis*-ordering along the *c*-axis in the wider range.

The content of oxygen and nitrogen has little influence on O/N ordering since both materials present a preference for *cis*-anionic ordering in a local range, and no anionic ordering in the long range. Only the coherence of the *cis*-ordering in LaTaO₂N is affected by the O/N content.

When it comes to the coherence length of the in-phase tilting along the *b*-axis in LaTaON₂, as seen in Table 4, the best fit up to 11 Å was always the one that took tilting into account. However, above 11 Å, the experimental data were best fitted by the *Imma* disordered structure. This may be an indication that the coherence length of tilting is about 1 nm, which may then be limited by antiphase boundaries that break the tilting correlation.

As for the fits of both compositions at 300 K, the conclusion is much the same as for the fits of the samples at 10 K: there is octahedral tilting along the *b*-axis and localized *cis*-ordering of the anions. Overall, the *R_w* values are lower (*R_w*(LaTaON₂) = 0.075; *R_w*(LaTaO₂N) = 0.064 at 1.5 Å ≤ *r* ≤ 5.5 Å); however, the peak broadening due to thermal vibrations makes it harder to distinguish between the different tested models.

A theoretical analysis was performed using the same approach described in the previous section. Figures S3 and S4 display the results for the obtained *Pnma* and *Pmn*2₁ crystal structures of LaTaON₂, respectively, in which the specific orbit indices representing the existing first-nearest-neighbor and second-nearest-neighbor configurations in each structure can be distinguished. The lattice parameters are summarized in Table S3. The results of the fittings of the elective cluster interactions of *Pnma* and *Pmn*2₁ LaTaON₂ can be seen in Figure S5 and Figure S6, respectively.

The Monte Carlo results depicted in Figure 9 support the results obtained by the PDF analysis, as they indicate a preference for a *cis*-configuration in LaTaON₂. Since the number of two-body N–N clusters in the second-nearest-neighbor configuration—represented by indices 11, 12, and 13 in Figure 9a and indices 21, 22, and 23 in Figure 9b—is lower than the number of two-body N–N clusters in the first-nearest-neighbor configuration—represented by indices 2, 3, and 4 in Figure 9a and indices 7, 8, and 9 in Figure 9b—including at our materials synthesis temperature of $T = 1275$ K, this indicates that for both *Pnma* and *Pmn2₁* LaTaON₂, there is a *cis*-configuration preference.

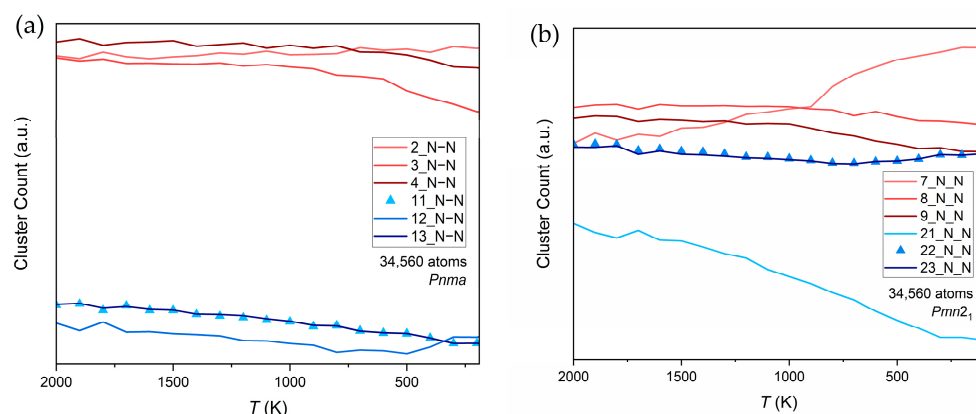


Figure 9. (a) Numbers of specific two-body clusters of *Pnma* LaTaON₂ at different temperatures and (b) numbers of specific two-body clusters of *Pmn2₁* LaTaON₂ at different temperatures.

In order to incorporate the effect of anionic ordering, a 40-atom special quasi-random-ordered (SQoS) [33,34] supercell was constructed by cluster correlation functions calculated at $T = 1750$ K, 1500 K, 1250 K, 1000 K, 750 K, and 500 K, as a representative structure in the space groups *Imma*, *Pnma*, and *Pmn2₁* LaTaON₂ at finite temperature. These temperatures were selected for the construction of the SQoS to cover a range from well above the synthesis temperature to well below it, providing insight into the ordering behavior across different thermal conditions, so as to simulate an annealing procedure.

The structurally relaxed SQoS energies of space groups *Imma*, *Pnma*, and *Pmn2₁* of LaTaON₂, which are temperature-dependent, are represented in Figure 10, and simulate representative structures characterized by a short-range order. As a reference, the special quasi-random (SQS) *Imma* supercell structure, depicted in a black dashed line in Figure 10, simulates a configurationally fully disordered system. The fundamental idea consisted of identifying a specific configuration within a given supercell, wherein the component atoms were distributed as randomly as possible. The SQS is temperature-independent. The energy comparison revealed that the ordered *Imma* structure had a significantly higher energy (~ 30 meV) compared to the SQS *Imma* supercell structure at $T = 1750$ K, indicating that the disordered *Imma* structure (represented by the SQS) is favored at very high temperatures, as observed in Figure 10. The energies of the SQoS *Pnma* and *Pmn2₁* structures are comparable to the disorder energy. As the temperature decreased towards 1000 K, the SQoS structure of *Imma* became progressively more stable. Overall, the three phases coexist at low temperatures and the energy difference (~ 30 meV) was of the same magnitude as the thermal fluctuation. At the synthesis temperature, $T = 1275$ K, the energies of all SQoS structures were comparable to the energy of the *Imma* disordered structure. This suggests no clear preference for either structure.

2.2.2. La_{0.9}Y_{0.1}Ta(O,N)₃

The same fitting process was applied to the PDF data of the Y-substituted compounds, La_{0.9}Y_{0.1}TaON₂ and La_{0.9}Y_{0.1}TaO₂N, and the overall features presented minimal change from the non-substituted to the isovalently substituted samples.

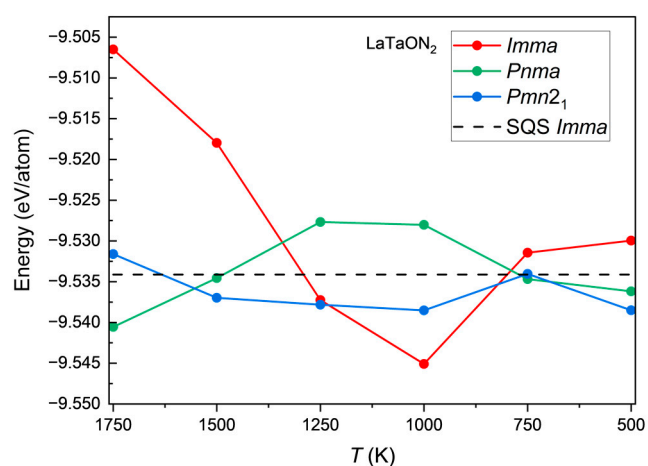


Figure 10. DFT energies of a special quasi-random-ordered (SQoS) supercell constructed for LaTaON₂ in the space groups *Imma*, *Pnma*, and *Pmn2*₁. The dashed line shows the special quasi-random (SQS) supercell energy of the *Imma* structure.

The addition of in-phase rotation of the octahedral network along the *b*-axis yielded good fits, as depicted in Figures 11a and 12a. A disordered model was observed in La_{0.9}Y_{0.1}TaON₂, whereas an inverse-ordered model was noted in La_{0.9}Y_{0.1}TaO₂N. The latter might have been caused by the 1:1 O/N ratio, as observed from the neutron diffraction data. Both compositions exhibited a *Pnma* (*a*⁻*b*⁺*a*⁻) tilting pattern, with corresponding *R_w* values that are summarized in Table 5. By applying local O/N ordering along the *c*-axis, the best fits in the local range were achieved, as illustrated in Figures 11b and 12b. These fits resulted in *R_w* values that are presented in Table 5.

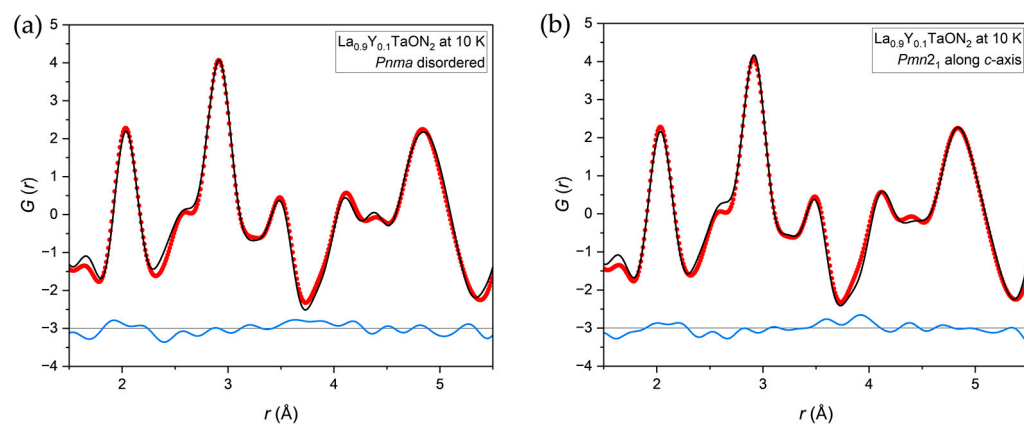


Figure 11. PDF pattern fits of (a) La_{0.9}Y_{0.1}TaON₂ at 10 K, with in-phase rotation of the octahedra along the *b*-axis, space group *Pnma*, and a disordered model, and (b) La_{0.9}Y_{0.1}TaON₂ at 10 K, with the addition of local O/N order along the *c*-axis and space group *Pmn2*₁. Both were in a 1.5 Å ≤ *r* ≤ 5.5 Å range. The red dots represent experimental data, the black line the calculated pattern, the blue line the difference curve, and the gray line is the offset zero line of the difference curve as serves as a guide to the eye.

When comparing the *Pnma* models with the models ordered along the *c*-axis, a slight fit improvement was observed for both compounds in the latter model. Furthermore, the *R_w* values of both materials slightly decreased in the shortest range when comparing the two different models.

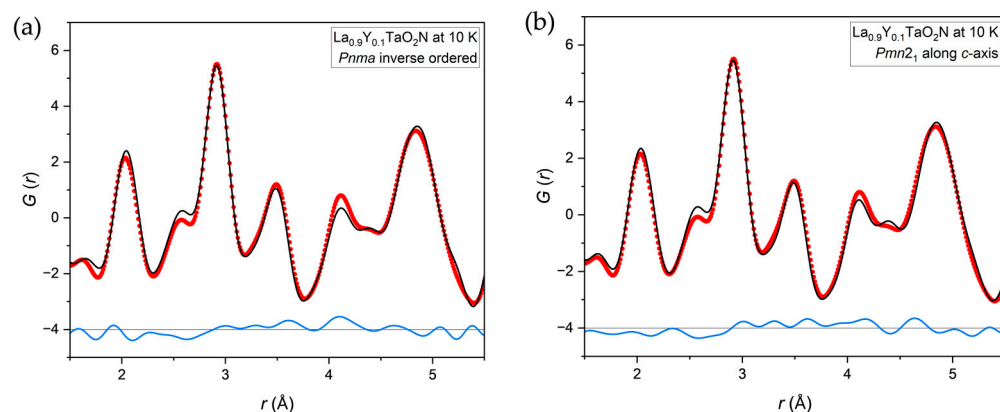


Figure 12. PDF pattern fits of (a) $\text{La}_{0.9}\text{Y}_{0.1}\text{TaO}_2\text{N}$ at 10 K, with in-phase rotation of the octahedra along the b -axis, space group $Pnma$, and an inverse-ordered model, and (b) $\text{La}_{0.9}\text{Y}_{0.1}\text{TaO}_2\text{N}$ at 10 K, with the addition of local O/N order along the c -axis and space group $Pmn2_1$. Both were in a $1.5 \text{ \AA} \leq r \leq 5.5 \text{ \AA}$ range. The red dots represent experimental data, the black line the calculated pattern, the blue line the difference curve, and the gray line is the offset zero line of the difference curve as serves as a guide to the eye.

Table 5. R_w values obtained using three distinct models in the PDF analysis for both $\text{La}_{0.9}\text{Y}_{0.1}\text{TaON}_2$ and $\text{La}_{0.9}\text{Y}_{0.1}\text{TaO}_2\text{N}$ at 10 K, in the short ($1.5 \text{ \AA} \leq r \leq 5.5 \text{ \AA}$) and wider ($1.5 \text{ \AA} \leq r \leq 11 \text{ \AA}$) ranges. The lowest values obtained for each composition are highlighted in bold.

Compound	Model	R_w ($1.5 \text{ \AA} - 5.5 \text{ \AA}$)	R_w ($1.5 \text{ \AA} - 11 \text{ \AA}$)
$\text{La}_{0.9}\text{Y}_{0.1}\text{TaON}_2$	<i>Imma</i> _disordered	0.124	0.140
	<i>Pnma</i> _disordered	0.107	0.130
	<i>Pmn2</i> ₁ _along- <i>c</i> -axis	0.101	0.132
$\text{La}_{0.9}\text{Y}_{0.1}\text{TaO}_2\text{N}$	<i>Imma</i> _disordered	0.124	0.152
	<i>Pnma</i> _inverse-ordered	0.108	0.133
	<i>Pmn2</i> ₁ _along- <i>c</i> -axis	0.105	0.127

Yttrium substitution did not alter the tilting pattern along the b -axis, which remained as $Pnma$ ($a^-b^+a^-$), nor did it affect the ordering patterns, as the local *cis*-ordering of the anions remained. However, as shown by the fits represented in Figures 11 and 12, isovalent substitution did introduce some additional disorder in the structure, affecting the quality of the fit and making the PDF analysis more challenging. This may indicate a dampening of the *cis*-ordering of the anions with the introduction of yttrium into the compounds, as is confirmed by the R_w values presented in Table 5, since in the $1.5 \text{ \AA} \leq r \leq 11 \text{ \AA}$ range, the R_w gets higher when compared to the shorter range and, in the case of $\text{La}_{0.9}\text{Y}_{0.1}\text{TaON}_2$, the lower R_w value was obtained by the $Pnma$ space group model in the widest range compared to $Pmn2_1$ in the shortest ($1.5 \text{ \AA} \leq r \leq 5.5 \text{ \AA}$) range.

3. Materials and Methods

3.1. Synthesis of LaTaO_2N and LaTaON_2

The oxynitrides LaTaO_2N and LaTaON_2 were synthesized from the respective precursor oxides via thermal ammonolysis, at $900 \text{ }^\circ\text{C}$ for 10 h, with an NH_3 gas flow rate of 300 mL/min ($>99.98\%$; Westfalen AG, Münster, Germany). A second ammonolysis cycle was carried out at $1000 \text{ }^\circ\text{C}$ for 14 h, using a KCl flux ($\geq 99\%$, Ph. Eur.; Carl Roth GmbH & Co. KG, Karlsruhe, Germany) with a sample-to-flux weight ratio of 1:1, as a way of contributing to a more homogeneous material and to a lower defect concentration, which enhances the material's purity and crystallinity [35,36]. Further details regarding the synthesis of the precursor oxides and the oxynitrides can be found in the study by Bubeck et al. [23].

3.2. Synthesis of $\text{La}_{0.9}\text{Y}_{0.1}\text{Ta}(\text{O},\text{N})_3$

The oxide precursors for $\text{La}_{0.9}\text{Y}_{0.1}\text{Ta}(\text{O},\text{N})_3$ were prepared by a sol-gel-related method with the addition of the appropriate amount of $\text{Y}(\text{NO}_3)_3 \cdot 6\text{H}_2\text{O}$ (99.9%; Alfa Aesar, Kandel, Germany) according to the 10 mol% fraction, as previously described in [10]. The oxynitride material was then synthesized from the respective precursor oxide via ex situ thermal ammonolysis, following the detailed procedure outlined in prior work [10]: at 950 °C for 10 h, under an NH_3 gas flow rate of 300 mL/min (>99.98%; Westfalen AG, Münster, Germany), followed by repeated ammonolysis cycles with KCl flux addition (weight ratio 1:1) at 1000 °C for 14 h until phase purity was achieved. Further information regarding the synthesis of the precursor oxides can be found in the study by Bubeck et al. [10].

3.3. Sample Characterization

Neutron diffraction experiments were performed using the D2B high-resolution powder diffractometer of the Institut Laue-Langevin in Grenoble, France, at both 10 K and 300 K, utilizing a Ge (335) monochromator and a take-off angle of 135°. The refined wavelength using a Si standard sample was 1.59417(2) Å. Samples were measured in 6 mm diameter vanadium cans at room temperature and at 10 K using a cryofurnace. All the neutron diffraction patterns obtained were refined by the Rietveld method [27,28], using the *Fullprof.2k* software (version 6.30) [29]. For the refinement, a pseudo-Voigt profile function was used with the Caglioti formula for the full width at half maximum (FWHM) determination, and the background was calculated using selected points with linear interpolation between them.

Data collection for pair distribution function analysis was carried out using the disordered-materials diffractometer D4c at the Institut Laue-Langevin (ILL) in Grenoble, France [37], at 10 K and 300 K, covering a Q -range up to 23.6 Å⁻¹. Each pattern summed up different scans for total counting times of ≈6 h. Empty cryostat, vanadium rod, empty cans, and boron powder patterns were also measured in order to properly subtract the background and normalize the data. The incident neutron wavelength $\lambda = 0.4959(3)$ Å was calculated using a Ni standard.

The local structural evolution was investigated through the PDF analysis, adopting the $G(r)$ formalism as described by Egami et al. [38]. The $G(r)$ was experimentally determined via sine Fourier transform of the total scattering function $S(Q)$, utilizing the proprietary software of D4c beamline [37]; and it indicates the probability of finding a pair of atoms separated by a distance r with an integrated intensity dependent on the pair multiplicity and the coherence scattering lengths of the elements involved. The data analysis took advantage of the large bound coherent scattering lengths of the “light” elements, nitrogen ($b_c = 9.36(2)$ fm) and oxygen ($b_c = 5.803(4)$ fm) [26], for neutron scattering and of the contrast between their two values. Modelling of PDF data was performed via PDFgui [39].

3.4. Density-Functional Theory Analysis

Density-functional theory analysis was performed using the cluster expansion method. Monte Carlo simulations based on the CE models were utilized. For each space group, a set of 300 configurations was generated, featuring O/N atoms randomly distributed within a 40-atom supercell.

The Kohn–Sham DFT, as implemented in the Vienna Ab initio Simulation Pack (VASP) was employed to ascertain the total energy of each configuration in their fully relaxed geometry. The interaction between valence and core electrons was addressed using the projector augmented wave (PAW) [40] method, in which the 5s and 5p states of La and the 5p states of Ta were used as valence electrons. A plane wave basis energy cutoff of 520 eV was established. The Perdew–Burke–Ernzerhof-for-solids (PBEsol) [41] density-functional approximation was applied for a better equilibrium lattice properties description. The Brillouin zone was densely sampled with 1000 k-points per reciprocal atom. The energy convergence criterion for self-consistent field iterations was meticulously set at 10⁻⁵ eV. Both unit cell parameters and internal atomic positions underwent optimization

through the conjugate gradient algorithm until the residual forces reached a threshold below $10 \text{ meV } \text{Å}^{-1}$.

The DFT-calculated energies from the randomly generated configurations were calculated and then integrated into the CE models through linear fitting, utilizing the automatic relevance detection regression (ARDR) algorithm implemented within the integrated cluster expansion toolkit (ICET) [32]. The Monte Carlo simulations were conducted using the MCHAMMER module of ICET. A significantly larger $12 \times 12 \times 12$ supercell was employed for these simulations, operating in the canonical ensemble. A simulated annealing procedure was adopted, where the temperature was gradually decreased from 2000 K to 0 K at a rate of 100 K per 100,000 MC cycles.

A 40-atom SQoS [33,34] supercell was constructed by using cluster correlation functions calculated at $T = 1750 \text{ K}$, 1500 K , 1250 K , 1000 K , 750 K , and 500 K , serving as a representative structure of *Imma*, *Pnma*, and *Pmn*₂₁ LaTaON₂ at finite temperature. Additionally, the SQS [42,43] supercell was considered to explore the possible configurational dependence of electronic properties of LaTaON₂. The construction of the SQS and SQoS was accomplished by the ICET.

4. Conclusions

The neutron diffraction analysis conducted on the (La,Y)Ta(O,N)₃ materials at 10 K and RT revealed that the best fit using the *Imma* random structural model indicated the absence of long-range O/N order in all of the compositions.

Pair distribution function analysis conducted on LaTa(O,N)₃ at 10 K and RT, as well as on La_{0.9}Y_{0.1}Ta(O,N)₃ at 10 K, revealed that starting with the long-range model, the best fit for $r > 11 \text{ Å}$ corresponded to the *Imma* average structure disordered model. When various anionic ordering patterns, including *trans*- and *cis*-orderings, were tested, the fits worsened, corroborating the conclusion drawn from the neutron diffraction analysis.

The summarized model of the anionic ordering suggests that in a longer distance range ($r > 11 \text{ Å}$), there is no discernible ordering of the anions; within the range of $1.5 \text{ Å} \leq r \leq 11 \text{ Å}$, a *Pnma* tilting pattern along the *b*-axis is observed, without any anionic ordering, and at a shorter range of $1.5 \text{ Å} \leq r < 6 \text{ Å}$, both the *Pnma* ($a^-b^+a^-$) tilting pattern and local *cis*-ordering of the anions are present. This conclusion was the same for all compositions studied, indicating that O/N content does not significantly influence anionic ordering, except for a wider ordering coherence observed in LaTaO₂N compared to LaTaON₂. These experimental findings are corroborated by the simulation experiments, which point as well to the absence of O/N ordering on the long range, in particular at higher temperatures, while the simulated annealing procedure using a MC approach revealed a preference for *cis*-ordering of the O and N on a local scale.

Yttrium substitution appeared to have minimal impact on octahedral tilting and O/N ordering in the structure. However, it did introduce some degree of disorder, as evidenced by the lower quality of fits obtained in the structural analysis. This suggested a dampening effect, especially on the anionic ordering.

The present study demonstrates that both LaTaON₂ and LaTaO₂N show similar behavior, characterized by the presence of local *cis*-ordering of the anions. Moreover, it suggests that anionic ordering does not significantly influence the band gap tunability resulting from Y-substitution. This finding emphasizes the stability of the band gap properties despite variations in anionic ordering, and might provide valuable insights into the future potential applications of these materials in optoelectronic devices.

Supplementary Materials: The following supporting information can be downloaded at: <https://www.mdpi.com/article/10.3390/inorganics12030090/s1>, Figure S1: Refined neutron diffraction patterns of (a) LaTaON₂, (b) LaTaO₂N, (c) La_{0.9}Y_{0.1}TaON₂, and (d) La_{0.9}Y_{0.1}TaO₂N at 10 K using the *Imma* random structural model; Figure S2: (a) ECIs for the cluster expansion energy of DFT energies, and (b) calculated and fitted DFT energies of the configurations of *Imma* LaTaON₂; Figure S3: Symmetrically non-equivalent two-body clusters in the cluster expansion of the total energy as a function of O/N occupation in *Pnma* LaTaON₂; Figure S4: Symmetrically non-equivalent two-body clusters in the

cluster expansion of the total energy as a function of O/N occupation in $Pmn2_1$ LaTaON₂; Figure S5: (a) ECIs for the cluster expansion energy of DFT energies, and (b) calculated and fitted DFT energies of the configurations of $Pnma$ LaTaON₂; Figure S6: (a) ECIs for the cluster expansion energy of DFT energies, and (b) calculated and fitted DFT energies of the configurations of $Pmn2_1$ LaTaON₂; Table S1: Rietveld refinement results of ND patterns at 300 K and 10 K of (a) LaTaON₂, (b) LaTaO₂N, (c) La_{0.9}Y_{0.1}TaON₂, and (d) La_{0.9}Y_{0.1}TaO₂N; Table S2: R_w values using distinct anisotropic thermal parameters in the PDF analysis for $Imma$ LaTaON₂ at 10 K; Table S3: Experimental and calculated lattice parameters of $Pnma$ and $Pmn2_1$ LaTaON₂, as determined by DFT analysis.

Author Contributions: Conceptualization, M.S., H.Z. and M.W.; data curation, C.B. and M.S.; formal analysis, M.D., C.B., M.S., G.J.C. and M.W.; funding acquisition, H.Z. and A.W.; investigation, M.D., C.B., M.S., G.J.C. and M.W.; methodology, M.B., M.D., C.B., M.S., G.J.C., H.Z. and M.W.; project administration, M.W.; resources, H.Z.; software, M.D.; supervision, H.Z., A.W. and M.W.; validation, M.D., H.Z. and M.W.; visualization, M.B.; writing—original draft, M.B.; writing—review and editing, M.D., C.B., M.S., H.Z., A.W. and M.W. All authors have read and agreed to the published version of the manuscript.

Funding: This research was funded by the German Research Council (DFG) within CRC 1548 (FLAIR), Grant No. 463184206 and SPP 1613 (SolarH2), Grant No. 198634447. M.S. acknowledges the financial support from the Università degli Studi di Milano (PSR2022_DIP_005_PI_AVERT_01 projects “Piano di Sostegno alla Ricerca 2022, Linea 2, Azione A”).

Data Availability Statement: All involved measurement and analysis data can be accessed from the corresponding authors upon justified request. The raw data collected on D2B and D4c at the ILL, Grenoble, France, are available under <https://doi.ill.fr/10.5291/ILL-DATA.6-06-482> accessed on 10 March 2024.

Acknowledgments: The authors kindly acknowledge the granted beam time by the ILL and the financial support received during the experiment. M.W. expresses his sincere thanks to Achim Diem, Christian Bäucker, and Lukas Link (University of Stuttgart) for their kind support during the sample preparation and the neutron diffraction experiments.

Conflicts of Interest: The authors declare no conflicts of interest.

References

1. Kubo, A.; Giorgi, G.; Yamashita, K. Anion Ordering in CaTaO₂N: Structural Impact on the Photocatalytic Activity. Insights from First-Principles. *Chem. Mater.* **2017**, *29*, 539–545. [[CrossRef](#)]
2. Ziani, A.; Le Paven, C.; Le Gendre, L.; Marlec, F.; Benzerga, R.; Tessier, F.; Chevire, F.; Hedhili, M.N.; Garcia-Esparza, A.T.; Melissen, S.; et al. Photophysical Properties of SrTaO₂N Thin Films and Influence of Anion Ordering: A Joint Theoretical and Experimental Investigation. *Chem. Mater.* **2017**, *29*, 3989–3998. [[CrossRef](#)]
3. Porter, S.H.; Huang, Z.; Woodward, P.M. Study of Anion Order/Disorder in RTa₂O (R = La, Ce, Pr) Perovskite Nitride Oxides. *Cryst. Growth Des.* **2014**, *14*, 117–125. [[CrossRef](#)]
4. Atfield, J.P. Principles and Applications of Anion Order in Solid Oxynitrides. *Cryst. Growth Des.* **2013**, *13*, 4623–4629. [[CrossRef](#)]
5. Clark, L.; Oró-Solé, J.; Knight, K.S.; Fuertes, A.; Atfield, J.P. Thermally Robust Anion-Chain Order in Oxynitride Perovskites. *Chem. Mater.* **2013**, *25*, 5004–5011. [[CrossRef](#)]
6. Ninova, S.; Aschauer, U. Anion-Order Driven Polar Interfaces at LaTiO₂N Surfaces. *J. Mater. Chem. A Mater.* **2019**, *7*, 2129–2134. [[CrossRef](#)]
7. Klein, A.; Albe, K.; Bein, N.; Clemens, O.; Creutz, K.A.; Erhart, P.; Frericks, M.; Ghorbani, E.; Hofmann, J.P.; Huang, B.; et al. The Fermi Energy as Common Parameter to Describe Charge Compensation Mechanisms: A Path to Fermi Level Engineering of Oxide Electroceramics. *J. Electroceram.* **2023**, *51*, 147–177. [[CrossRef](#)]
8. Young, S.D.; Chen, J.; Sun, W.; Goldsmith, B.R.; Pilia, G. Thermodynamic Stability and Anion Ordering of Perovskite Oxynitrides. *Chem. Mater.* **2023**, *35*, 5975–5987. [[CrossRef](#)]
9. Jansen, M.; Letschert, H.P. Inorganic Yellow-Red Pigments without Toxic Metals. *Nature* **2000**, *404*, 980–982. [[CrossRef](#)]
10. Bubeck, C.; Bubeck, C.; Widenmeyer, M.; De Denko, A.T.; Richter, G.; Coduri, M.; Coduri, M.; Colera, E.S.; Colera, E.S.; Goering, E.; et al. Bandgap-Adjustment and Enhanced Surface Photovoltage in Y-Substituted LaTa^{IV}O₂N. *J. Mater. Chem. A Mater.* **2020**, *8*, 11837–11848. [[CrossRef](#)]
11. Wang, C.H.; Kennedy, B.J.; Menezes De Oliveira, A.L.; Polt, J.; Knight, K.S. The Impact of Anion Ordering on Octahedra Distortion and Phase Transitions in SrTaO₂N and BaTaO₂N. *Acta Crystallogr. B Struct. Sci. Cryst. Eng. Mater.* **2017**, *73*, 389–398. [[CrossRef](#)]
12. Zhao, Z.C.; Yang, C.L.; Meng, Q.T.; Wang, M.S.; Ma, X.G. Strain Effect on the Electronic and Optical Properties of ATaO₂N (A = Ca, Sr, and Ba): Insights from the First-Principles. *Appl. Phys. A Mater. Sci. Process* **2019**, *125*, 789. [[CrossRef](#)]

13. Vonrüti, N.; Aschauer, U. Epitaxial Strain Dependence of Band Gaps in Perovskite Oxynitrides Compared to Perovskite Oxides. *Phys. Rev. Mater.* **2018**, *2*, 105401. [CrossRef]
14. Yang, M.; Oró-Solé, J.; Kusmartseva, A.; Fuertes, A.; Attfield, J.P. Electronic Tuning of Two Metals and Colossal Magnetoresistances in $\text{EuWO}_{1+x}\text{N}_{2-x}$ Perovskites. *J. Am. Chem. Soc.* **2010**, *132*, 4822–4829. [CrossRef]
15. Johnston, H.; Black, A.P.; Kayser, P.; Oró-Solé, J.; Keen, D.A.; Fuertes, A.; Paul Attfield, J. Dimensional Crossover of Correlated Anion Disorder in Oxynitride Perovskites. *Chem. Commun.* **2018**, *54*, 5245–5247. [CrossRef]
16. Ebbinghaus, S.G.; Weidenkaff, A.; Rachel, A.; Reller, A. Powder Neutron Diffraction of SrNbO_2N at Room Temperature and 1.5 K. *Acta Crystallogr. C* **2004**, *60*, i91–i93. [CrossRef] [PubMed]
17. Clarke, S.J.; Hardstone, K.A.; Michie, C.W.; Rosseinsky, M.J. High-Temperature Synthesis and Structures of Perovskite and $n = 1$ Ruddlesden-Popper Tantalum Oxynitrides. *Chem. Mater.* **2002**, *14*, 2664–2669. [CrossRef]
18. Günther, E.; Hagenmayer, R.; Jansen, M. Strukturuntersuchungen an Den Oxidnitriden SrTaO_2N , CaTaO_2N Und LaTaON_2 Mittels Neutronen- Und Röntgenbeugung. *J. Inorg. Gen. Chem.* **2000**, *626*, 1519–1525. [CrossRef]
19. Page, K.; Stoltzfus, M.W.; Kim, Y.I.; Proffen, T.; Woodward, P.M.; Cheetham, A.K.; Seshadri, R. Local Atomic Ordering in BaTaO_2N Studied by Neutron Pair Distribution Function Analysis and Density Functional Theory. *Chem. Mater.* **2007**, *19*, 4037–4042. [CrossRef]
20. Wolff, H.; Dronskowski, R. First-Principles and Molecular-Dynamics Study of Structure and Bonding in Perovskite-Type Oxynitrides ABO_2N ($A = \text{Ca, Sr, Ba}$; $B = \text{Ta, Nb}$). *J. Comput. Chem.* **2008**, *29*, 2260–2267. [CrossRef] [PubMed]
21. Kikkawa, S.; Sun, S.; Masubuchi, Y.; Nagamine, Y.; Shibahara, T. Ferroelectric Response Induced in Cis-Type Anion Ordered SrTaO_2N Oxynitride Perovskite. *Chem. Mater.* **2016**, *28*, 1312–1317. [CrossRef]
22. Hinuma, Y.; Moriwake, H.; Zhang, Y.-R.; Motohashi, T.; Kikkawa, S.; Tanaka, I. First-Principles Study on Relaxor-Type Ferroelectric Behavior without Chemical Inhomogeneity in BaTaO_2N and SrTaO_2N . *Chem. Mater.* **2012**, *24*, 2023. [CrossRef]
23. Bubeck, C.; Widenmeyer, M.; Richter, G.; Coduri, M.; Goering, E.; Yoon, S.; Weidenkaff, A. Tailoring of an Unusual Oxidation State in a Lanthanum Tantalum(IV) Oxynitride via Precursor Microstructure Design. *Commun. Chem.* **2019**, *2*, 134. [CrossRef]
24. Kageyama, H.; Hayashi, K.; Maeda, K.; Attfield, J.P.; Hiroi, Z.; Rondinelli, J.M.; Poeppelmeier, K.R. Expanding Frontiers in Materials Chemistry and Physics with Multiple Anions. *Nat. Commun.* **2018**, *9*, 772. [CrossRef]
25. Coppens, P. The Effect of Thermal Vibrations on the Intensities of the Diffracted Beams. In *X-ray Charge Densities and Chemical Bonding*; Oxford Academic Press: New York, NY, USA, 1997. [CrossRef]
26. Prince, E. (Ed.) *International Tables for Crystallography*, 3rd ed.; Kluwer Academic Publishers: Dordrecht, The Netherlands, 2004; Volume C, ISBN 978-0-470-71029-6.
27. Rietveld, H.M. Line Profiles of Neutron Powder-Diffraction Peaks for Structure Refinement. *Acta Cryst.* **1967**, *22*, 151–152. [CrossRef]
28. Rietveld, H.M. A Profile Refinement Method for Nuclear and Magnetic Structures. *J. Appl. Cryst.* **1969**, *2*, 65–71. [CrossRef]
29. FullProf Suite Homepage. Available online: <https://www.ill.eu/sites/fullprof/> (accessed on 9 February 2024).
30. Kresse, G.; Furthmüller, J. Efficiency of *Ab-Initio* Total Energy Calculations for Metals and Semiconductors Using a Plane-Wave Basis Set. *Comput. Mater. Sci.* **1996**, *6*, 15–50. [CrossRef]
31. Kresse, G.; Furthmüller, J. Efficient Iterative Schemes for *Ab Initio* Total-Energy Calculations Using a Plane-Wave Basis Set. *Phys. Rev. B* **1996**, *54*, 11169. [CrossRef]
32. Ångqvist, M.; Muñoz, W.A.; Rahm, J.M.; Fransson, E.; Durniak, C.; Rozyczko, P.; Rod, T.H.; Erhart, P. ICET—A Python Library for Constructing and Sampling Alloy Cluster Expansions. *Adv. Theory Simul.* **2019**, *2*, 1900015. [CrossRef]
33. Saitta, A.M.; de Gironcoli, S.; Baroni, S. Structural and Electronic Properties of a Wide-Gap Quaternary Solid Solution: $(\text{Zn, Mg})(\text{S, Se})$. *Phys. Rev. Lett.* **1998**, *80*, 4939. [CrossRef]
34. Liu, J.; Fernández-Serra, M.V.; Allen, P.B. First-Principles Study of Pyroelectricity in GaN and ZnO . *Phys. Rev. B* **2016**, *93*, 081205. [CrossRef]
35. Fuertes, A. Synthetic Approaches in Oxynitride Chemistry. *Prog. Solid State Chem.* **2018**, *51*, 63–70. [CrossRef]
36. Kim, Y. II Effects of KCl Flux on the Morphology, Anion Composition, and Chromaticity of Perovskite Oxynitrides, CaTaO_2N , SrTaO_2N , and LaTaON_2 . *Ceram. Int.* **2014**, *40*, 5275–5281. [CrossRef]
37. Fischer, H.E.; Cuello, G.J.; Palleau, P.; Feltin, D.; Barnes, A.C.; Badyal, Y.S.; Simonson, J.M. D4c: A Very High Precision Diffractometer for Disordered Materials. *Appl. Phys. A Mater. Sci. Process* **2002**, *74*, s160–s162. [CrossRef]
38. Egami, T.; Billinge, S.J.L. *Underneath the Bragg Peaks-Structural Analysis of Complex Materials*, 2nd ed.; Elsevier: Oxford, UK, 2012; Volume 16.
39. Farrow, C.L.; Juhas, P.; Liu, J.W.; Bryndin, D.; Boin, E.S.; Bloch, J.; Proffen, T.; Billinge, S.J.L. PDFfit2 and PDFgui: Computer Programs for Studying Nanostructure in Crystals. *J. Phys. Condens. Matter* **2007**, *19*, 335219. [CrossRef]
40. Blöchl, P.E.; Jepsen, O.; Andersen, O.K. Improved Tetrahedron Method for Brillouin-Zone Integrations. *Phys. Rev. B* **1994**, *49*, 16223. [CrossRef]
41. Perdew, J.P.; Ruzsinszky, A.; Csonka, G.I.; Vydrov, O.A.; Scuseria, G.E.; Constantin, L.A.; Zhou, X.; Burke, K. Restoring the Density-Gradient Expansion for Exchange in Solids and Surfaces. *Phys. Rev. Lett.* **2008**, *100*, 136406. [CrossRef]

-
42. Wei, S.H.; Ferreira, L.G.; Bernard, J.E.; Zunger, A. Electronic Properties of Random Alloys: Special Quasirandom Structures. *Phys. Rev. B* **1990**, *42*, 9622. [[CrossRef](#)]
 43. Zunger, A.; Wei, S.H.; Ferreira, L.G.; Bernard, J.E. Special Quasirandom Structures. *Phys. Rev. Lett.* **1990**, *65*, 353. [[CrossRef](#)]

Disclaimer/Publisher's Note: The statements, opinions and data contained in all publications are solely those of the individual author(s) and contributor(s) and not of MDPI and/or the editor(s). MDPI and/or the editor(s) disclaim responsibility for any injury to people or property resulting from any ideas, methods, instructions or products referred to in the content.